

Subpacket Structure in Strong VLF Chorus Rising Tones: Characteristics and Consequences for Radiation Belt Acceleration

John C. Foster (✉ jcfoster@mit.edu)

Massachusetts Institute of Technology Haystack Observatory <https://orcid.org/0000-0002-1993-241X>

Philip J. Erickson

Massachusetts Institute of Technology Haystack Observatory

Yoshiharu Omura

Kyoto University - Uji Campus: Kyoto Daigaku - Uji Campus

Research Article

Keywords: VLF chorus, subpackets

Posted Date: February 10th, 2021

DOI: <https://doi.org/10.21203/rs.3.rs-227425/v1>

License:  This work is licensed under a Creative Commons Attribution 4.0 International License.

[Read Full License](#)

Version of Record: A version of this preprint was published at Earth, Planets and Space on July 7th, 2021.
See the published version at <https://doi.org/10.1186/s40623-021-01467-4>.

Abstract

Van Allen Probes in situ observations are used to examine detailed subpacket structure observed in strong VLF (very low frequency) rising tone chorus elements observed at the time of a rapid MeV electron energization in the inner magnetosphere. Analysis of the frequency gap between lower and upper chorus-band waves identifies f_{ceEQ} , the electron gyrofrequency in the equatorial wave generation region. Initial subpackets in these strong chorus rising-tone elements begin at a frequency near $1/4 f_{ceEQ}$, exhibit smooth gradual frequency increase across their > 10 ms temporal duration. A second much stronger subpacket is seen at frequencies around the local value of $1/4 f_{ce}$ with small wave normal angle (< 10 deg) and steeply rising df/dt . Smooth frequency and phase variation across and between the initial subpackets supports continuous phase trapping of resonant electrons and increased potential for MeV electron acceleration. The total energy gain for seed electrons with energies between 100 keV and 3 MeV ranges between 2 % and 15 %, in their nonlinear interaction with a single chorus element.

Introduction

Rapid recovery (30-min; 10x increase) of Earth's radiation belt MeV electron fluxes following a storm-induced dropout have been reported (Baker 2014; Foster et al 2014). Such rapid acceleration is associated with low energy (10s-100s keV) electron injection, local acceleration (Reeves et al., 2013), and strong VLF chorus rising tones (risers) (Thorne et al., 2013). Jaynes et al. (2015) have shown that two distinct electron populations resulting from magnetospheric substorm activity are essential for the overall mechanism leading to acceleration of highly relativistic electrons in the outer belt: (1) a source population of injected tens of keV electrons that drive VLF wave growth, and (2) a seed population at hundreds of keV that are then accelerated by these VLF waves to MeV energies. The structure and acceleration efficiency of the chorus wave elements is important for understanding this process. The Van Allen Probes twin spacecraft (Mauk et al., 2012) were well positioned in the inner magnetosphere to observe the characteristics of the chorus waves involved in the 17 March 2013 radiation belt recovery event (Baker et al., 2014; Foster et al., 2014).

Subpacket structure in chorus wave elements

A typical chorus emission consists of a coherent wave with rising frequency (rising-tones). Each chorus element is composed of a sequence of discrete subpackets, each spanning a few to several 10s of wave cycles. In general, each subpacket is characterized by smoothly increasing and decreasing wave amplitude, good coherence, and regularly varying wave frequency (e.g. Santolik et al., 2014). The initial part of the chorus emission at lower frequency results from linear instability driven by a temperature anisotropy which develops during electron injection into the inner magnetosphere. When the growing wave amplitude attains a threshold amplitude (Omura et al (2009); Omura & Nunn (2011)), the wave packet grows through a nonlinear process associated with the formation of an electromagnetic electron hole in velocity phase space (Omura et al., 2008). The source of the wave packet growth is primarily the frequency variation induced by the electron hole. For nonlinear chorus wave growth, the inhomogeneity

factor, S , is important ($S \sim -0.4$ for optimal wave amplitude). S depends on df/dt , dB_o/dx and inversely on wave power (Omura et. al., 2008).

At the equatorial source region, where dB_o/dx is small, nonlinear wave growth is directly proportional to df/dt . As the wave packet propagates away from the equator, its frequency structure remains the same, while wave amplitude increases with dB_o/dx in a convective wave growth scenario. Once the wave amplitude exceeds the optimum wave amplitude (Omura and Nunn, 2011), the wave growth saturates, and the amplitude decreases gradually. In general, new seed waves are generated upstream from the equator by approaching resonant electrons with velocity towards the equator and whose phase has been modulated with the frequency of the preceding saturated wave packet. This packet has by definition a frequency higher than that of the original triggering wave. In the resulting interaction, the phase-modulated electrons generate a new triggering wave at the higher frequency. This wave growth process is repeated many times, forming a chorus element with a sequence of subpackets at progressively higher frequencies (Shoji and Omura, 2013). We note an important feature of this overall sequence: the wave frequency at any point in the chorus element is fixed in the near-equatorial generation region and does not vary as the wave packet propagates away from the equator. However, wave amplitude, as noted above, can vary as the wave propagates to its point of observation on an *in-situ* platform.

Characteristics of strong subpackets

Large amplitude whistler-mode chorus waves were first reported by Cattell et al (2008). Santolik et al. (2014) found fine structure in such chorus elements, with peak instantaneous amplitudes occasionally reaching up to 3 nT. That study also found the wave vector to be quasi-parallel to the background magnetic field for large-amplitude subpackets, with a distinct turn away from this direction when amplitudes are weaker. In a statistical analysis of intense lower-band chorus wave subpackets, Zhang et al. (2020) investigated the relationships between wave frequency variations, packet length, and wave amplitude, and their temporal variability. They found that 15% of the wave power is carried by long subpackets with low frequency sweep rates that agree well with the nonlinear theory of chorus wave growth. The remaining 85% of the wave power is associated with short packets with large frequency variations around the overall linear trend.

In this study, we use Van Allen Probes in situ observations to examine detailed subpacket structure observed in strong VLF rising tone chorus elements observed at the time of a rapid (30 min) MeV electron energization in the inner magnetosphere at $L \sim 4$, previously discussed by Foster et al. (2014, 2016). We analyze local in-situ wave electric and magnetic field observations made with the Electric and Magnetic Field Instrument and Integrated Science (EMFISIS) instrument (Kletzing et al., 2012), following the methods introduced by Foster et al. (2016). Because the spacecraft is situated at a non-zero magnetic latitude, the observations occur after the wave packets have propagated some distance from their origin in the equatorial region. As described below, both local and equatorial conditions are important for understanding the characteristics of observed subpackets, and therefore in the following analysis we

differentiate between f_{ce} , the local electron gyrofrequency measured at the point of observation, and f_{ceEQ} , the equatorial electron gyrofrequency. Our determination of f_{ceEQ} is described below.

Figure 1 presents Van Allen Probes EMFISIS observations of a strong VLF chorus element observed during the March 17, 2013 event previously discussed by Foster et al. (2014). The upper panel (a) shows the magnitude of the wave magnetic field perpendicular to the wave propagation direction, \mathbf{k} , and the wave frequency determined over each 1/2 wave cycle. Panel (b) presents the wave power spectrogram for one component (B_u) of the chorus wave magnetic field. The strong chorus element in Figure 1 began with an extended (>50 ms) interval of weak wave amplitude with nearly constant frequency, preceding the onset of nonlinear wave growth. A sequence of subpackets with increasing wave frequency and variable amplitude followed.

Observations during the March 17, 2013 event suggest that the initial period of wave growth occurred at or slightly below $\sim 1/4 f_{ceEQ}$ (see following discussion for f_{ceEQ} determination procedure). Figure 2 presents a wave property analysis of the initial subpackets for four strong chorus elements, typical of those observed while rapid MeV radiation belt electron acceleration was taking place during the event. For each of the individual chorus elements (a, b, c, d), the magnetic field waveform is shown in the upper panel, and shown sequentially below are the magnitude of E_R , the normalized frequency (f/f_{ce}), and the wave normal angle ($WNA = \arccos(\mathbf{k} \cdot \mathbf{B}_0)$). Wave frequency and wave normal angle are calculated at each 1/2 wave cycle following the procedure described by Foster et al. (2016). (Note that no frequency domain filtering has been applied to the observed waveform, with the result that stronger overlapping signals from other emissions could disrupt the wave cycle frequency analysis.)

In each case shown here, the onset of the first nonlinear subpacket is accompanied by a decrease of wave normal angle ($WNA < 20$ deg), is of extended duration (20 ms - 30 ms), exhibits slowly rising wave frequency and amplitude, and often begins near $1/4 f_{ceEQ}$. A second much stronger subpacket (see above) is seen at frequencies around $1/4 f_{ce}$ with low wave normal angle ($WNA < 10$ deg) and steeply rising df/dt . For the cases shown in Figure 2, wave frequency and phase vary smoothly both within the 1st and 2nd subpackets and across the transition between them. Peak wave magnetic field amplitudes of 1 - 2 nT ($E_R \sim 50 - 100$ mV/m) and subpacket durations of ~ 10 ms are typical for the strong 2nd subpackets. Additional descriptive characteristics of the subpackets denoted "A" and "B" in panel b are presented in Table 1.

Frequency span of lower band risers

At locations away from the equator, chorus elements are divided into lower and upper band emissions by a pronounced amplitude minimum below the local value $1/2 f_{ce}$. This feature occurs as the wave packet propagates into regions of increasing magnetic field where damping at $1/2 f_{ce}$ progressively erodes wave amplitude at frequencies above $1/2 f_{ceEQ}$. The wave power damping seen in Figure 3 between $1/2$ the local and $1/2$ the equatorial electron cyclotron frequency is in keeping with the nonlinear damping mechanism described by Hsieh and Omura (2018). Integrated signal power across the ~ 400 ms of observations

shown in panel (a) clearly identifies $1/2 f_{ce}$ in the equatorial chorus generation region as the point of onset of the $\sim 1000x$ decrease in the chorus element integrated wave power. Thus determined, the value of f_{ceEQ} also indicates that the frequency of initial chorus element wave growth occurred near $1/4 f_{ceEQ}$.

Figure 4 presents a cycle by cycle analysis of the subpacket structure for the chorus element shown in Figure 3. Many characteristics are similar to those discussed in Figure 2. Here wave frequency normalized by f_{ceEQ} is shown. Coherent nonlinear wave growth and steadily increasing frequency began at 20.18 s near $1/4 f_{ceEQ}$ as WNA drops < 10 deg. The initial period of wave growth "C" extends for ~ 65 ms, followed by a 10 ms strong 2nd subpacket "D". Wave amplitude decreased significantly between subpackets in this example, observed by RBSP-B during the same substorm injection event as the chorus element shown in Figure 2b. The substorm events at 16 UT and 22 UT on March 17, 2013 were described by Foster et al (2016).

Table 1 enumerates and compares the characteristics and ambient conditions associated with chorus elements (A, B, C, and D) discussed above.

Radiation belt effects

The growth of rising-frequency chorus elements involves nonlinear cyclotron resonance ($n = 1$) with 10s to 100s keV electrons that are injected into the inner magnetosphere during substorm dipolarization events (e.g. Foster, Rosenberg and Lanzerotti (1976); Foster et al., (2014)). As shown by analysis of simulations reproducing chorus emissions, the resonant current is mostly due to the nonlinear motion of resonant electrons moving slowly around the separatrix of the nonlinear trapping potential, resulting in formation of an electron hole. These untrapped resonant electrons are decelerated by the wave electric field, transferring energy to the wave. During this interaction, perpendicular particle velocities and pitch angles are decreased substantially, such that these particles precipitate into the loss cone through their interaction with an individual chorus element (e.g. Foster and Rosenberg (1976)). For the March 17, 2013 event described by Foster et al. (2014, 2016), strong chorus wave enhancement accompanied substorm events with onsets near 16 UT and 22 UT. Electron fluxes from the Magnetic Electron Ion Spectrometer (MagEIS; Blake et al., 2013) and Helium, Oxygen, Proton, and Electron (HOPE) mass spectrometer (Funsten et al., 2013) instruments, shown in Figure 5, characterized the discrete injections of electrons at the resonant energies ($n = 1$; 10 - 20 deg pitch angle) associated with the chorus elements described above in Figures 2 and 4. At the same time, the growing chorus waves serve as intermediaries for energy transfer from the lower energy injected particles to a pre-existing seed population of higher energy radiation belt electrons, as described by Jaynes et al. (2015).

Nonlinear interactions between 100s keV seed electrons and chorus waves were investigated by Foster et al. (2016) using burst mode EMFISIS observations of individual risers. That study concluded that nonlinear cyclotron resonance with parallel-propagating chorus waves could explain the rapid enhancement of MeV electron fluxes (10x over 30 min) observed during the 17 March 2013 event. Hsieh and Omura (2018) and Omura et al. (2019) extended theoretical analysis of the nonlinear energization

potential of VLF chorus rising tones to the case of obliquely-propagating waves (e.g. Santolik et al. (2009)), including both cyclotron ($n = 1$) and Landau ($n = 0$) interactions. They found that nonlinear trapping of relativistic electrons by the Lorentz force of the perpendicular wave magnetic field resulted in effective electron acceleration (Omura et al., 2019). Furthermore, Higara and Omura (2020) investigated the nonlinear trapping of seed electrons with multiple subpackets within a single chorus element and described the finite probability of an electron being trapped (and accelerated) for 10s of milliseconds through multiple sequential subpackets.

We apply the energy gain formulas developed by Omura et al. (2019) to individual riser subpackets (A, B, C, and D, denoted above in Figures 2b and 4) during the 17 March 2013 event. These strong subpackets have temporal durations of 20 - 70 ms (20 - 50 wave cycles; see Table 1) and produce a maximum energy gain of 5-10 keV/wave cycle for trapped electrons with 1-3 MeV initial energy. Figure 6 presents the calculated percent energy gain for seed electrons with initial energies between 30 keV and 10 MeV during the individual first (gradual) or second (strong) nonlinear subpackets for each of the two chorus elements discussed above in Figures 2b and 4.

Results indicate that for electrons resonant with the waves throughout a single subpacket (~ 10 ms), total energy increase of >100 keV is possible. Energy increase from cyclotron ($n = 1$) and Landau ($n = 0$) effects is of similar magnitude, with Landau effects usually the larger contributor at relativistic energies. Finally, 1 MeV seed electrons can experience a 1% - 3% energy gain in their interaction with a single strong chorus element subpacket.

Discussion

Prominent in our observations of strong chorus elements is a large-amplitude 2nd subpacket with steep df/dt near $1/4 f_{ce}$ as measured at the spacecraft location. We suggest two causes for these characteristics. First, the wave group velocity maximizes at frequencies near the local value of $1/4 f_{ce}$. As constant-frequency wave elements propagate away from equator, frequencies near $1/4 f_{ce}$ catch up with lower frequency wave elements emitted at an earlier time in the initial frequency dispersed (chirped) emission generated at the equator. Second, the observed decrease in wave normal angle as the wave amplitude increases leads to a further increase in parallel propagation velocity for frequencies near $1/4 f_{ce}$. Both these effects contribute to a “piling up” of wave power (analogous to “de-dispersion”) and an effective increase of df/dt at the off-equator observing position.

For strong subpackets, smooth wave frequency and phase variation with decreased but non-zero wave amplitude occurs between subpackets (cf. Figure 2). In Figures 2 and 4, small frequency decreases are observed between these initial subpackets. This effect has been predicted in a recent paper by Hanzelka et al. (2020), who used nonlinear growth theory of chorus emissions to develop a simple model of subpacket formation.

We note that there is little indication of discontinuous frequency jumps at subpacket boundaries. This is most apparent between subpackets 1 and 2, and in particular suggests good continuity of electron phase trapping between those subpackets along with good overall potential for MeV acceleration (e.g Higara and Omura (2020)). Figure 7 plots the total percent energy gain for seed electrons trapped across both 1st and 2nd subpackets for the four chorus elements shown in Figure 2. For the three chorus risers (a, c, and d) observed near $L \sim 5$ during the 16 UT radiation belt acceleration event, the total energy gain for seed electrons between 100 keV and 3 MeV ranges between 2 % and 15 %, obtained through their nonlinear interaction with the single chorus element.

Tsurutani et al. (2020) described rising-tone chorus elements composed of coherent approximately “monochromatic” steps, instead of a gradual sweep in frequency over the whole element. By contrast, subpackets shown here in Figures 1, 2, and 4 exhibit a very clear frequency increase during the growth of individual subpackets. A possible explanation for this difference lies in the longer duration (>10 ms) of the initial subpackets we study here. The statistical study of Zhang et al. (2020) noted that only 15% of the total wave power in strong chorus elements is carried in such long subpackets. In Figure 8, we further examine the overall chorus element in Figure 2(a) by showing an extended (80 ms) time interval including the first five subpackets. Right-hand whistler mode wave magnetic field amplitude (B_r), normalized wave frequency, and wave normal angle are shown, and the initial 5 subpackets each reach maximum amplitude of 1 nT or greater. For this chorus element, the longer-duration subpackets (1, 2, and 5) exhibit smoothly rising frequency across their temporal extent, while a step-like frequency plateau characterizes the shorter subpackets (3 and 4).

Summary And Conclusions

Repeatable initial subpacket structure in strong chorus elements observed during rapid radiation belt acceleration events features coherent temporal durations of 10 ms to 30 ms and peak wave magnetic field amplitudes of 1 - 2 nT ($E_R \sim 50 - 100$ mV/m). As constant-frequency wave elements propagate away from equator into regions of increasing magnetic field, damping at $1/2 f_{ce}$ progressively erodes wave amplitude at frequencies above $1/2 f_{ceEQ}$. Observed off the equator, an initial long (> 20 ms) coherent subpacket exhibits slowly rising frequency, wave normal angle < 20 deg, and frequency onset near $1/4 f_{ceEQ}$. A second stronger subpacket centered near $1/4 f_{ce}$ at the point of observation exhibits rapidly rising frequency (df/dt) and small (< 10 deg) wave normal angle. Wave frequency and phase vary smoothly both within these 1st and 2nd subpackets and across the transition between them providing appropriate conditions for continuous resonant electron phase trapping, leading to good potential for MeV electron acceleration. Maximum energy gain of 5-10 keV/wave cycle is calculated for electrons with 1-3 MeV initial energy.

Abbreviations

EMFISIS : Electric and Magnetic Field Instrument and Integrated Science

HOPE: Helium, Oxygen, Proton, and Electron mass spectrometer

MagEIS: Magnetic Electron Ion Spectrometer

VLf: very low frequency

WNA: wave normal angle

Declarations

Ethics approval and consent to participate

Not applicable

Consent for publication

Not applicable

Availability of data and materials

Van Allen Probes observations used in this study can be obtained through instrument websites (EMFISIS wave data: <http://emfisis.physics.uiowa.edu>; MagEIS and HOPE particle data: https://rbsp-ect.lanl.gov/rbsp_ect.php). The values of electron energy gain shown in Figures 6 and 7 are calculated from equations (72) and (73) of Omura et al. (2019).

Competing interests

Not applicable

Funding

Research at the MIT Haystack Observatory was supported by the NASA Van Allen Probes (RBSP) funding provided under NASA prime contract NAS5-01072, including the EFW investigation (PI: J.R. Wygant, University of Minnesota), and the ECT investigation (PI: H. Spence, University of New Hampshire). The work at Kyoto University is supported by JSPS KAKENHI grant 17H06140.

Authors' contributions

JF proposed and outlined the study and led the data analysis, scientific interpretation, and manuscript preparation. PE selected and prepared the high-resolution data used in the study and collaborated closely on their interpretation and presentation. YO provided suggestions, guidance and discussion on nonlinear wave development and other theoretical perspectives. All authors read and approved the final manuscript.

Acknowledgements

We thank C. Kletzing and the EMFISIS team for providing the high resolution EMFISIS burst mode data.

Authors' information

Not applicable

Endnotes

Not applicable

References

Baker DN, Foster JC, Erickson PJ, et al. (2014), Gradual Diffusion and Punctuated Phase Space Density Enhancements of Highly Relativistic Electrons: Van Allen Probes Observations, *Geophys Res Lett*, DOI: 10.1002/2013GL058942.

Blake JB, et al. (2013), Magnetic Electron Ion Spectrometer (MagEIS) instruments aboard the Radiation Belt Storm Probes (RBSP) spacecraft, *Space Sci Rev*, doi:10.1007/s11214-013-9991-8.

Cattell C, Wygant JR, Goetz K, et al. (2008), Discovery of very large amplitude whistler-mode waves in Earth's radiation belts, *Geophys Res Lett*, 35, L01105, doi:10.1029/2007GL032009.

Foster JC, and Rosenberg TJ (1976), Electron precipitation and VLF emissions associated with cyclotron resonance interactions near the plasmopause *J Geophys Res*, 81(13), 2183–2192, doi:10.1029/JA081i013p02183.

Foster JC, Rosenberg TJ, and Lanzerotti LJ (1976), Magnetospheric conditions at the time of enhanced wave-particle interactions near the plasmopause, *J Geophys Res*, 81(13), 2175-2182, doi: 10.1029/JA081i013p02175.

Foster JC, Erickson PJ, Baker DN, et al (2014), Prompt energization of relativistic and highly relativistic electrons during substorm intervals: Van Allen Probes observations, *Geophys Res Lett*, 41, 20-25, DOI: 10.1002/2013GL058438.

Foster JC, Erickson PJ, Omura Y, et al. (2017) Van Allen Probes observations of prompt MeV radiation belt electron acceleration in nonlinear interactions with VLF chorus. *J Geophys Res Space Phys*. <https://doi.org/10.1002/2016JA023429>

Funsten HB, Skoug RM, Guthrie AA, et al. (2013), Helium, Oxygen, Proton, and Electron (HOPE) mass spectrometer for the Radiation Belt Storm Probes Mission, *Space Sci Rev.*, 179, 423–484, doi:10.1007/s11214-013-9968-7.

Hanzelka M, Santolík O, Omura, et al. (2020), A model of the subpacket structure of rising tone chorus emissions, *J Geophys Res Space Phys*, 125, e2020JA028094. <https://doi.org/10.1029/2020JA028094>.

- Hiraga R, and Omura Y (2020), Acceleration mechanism of radiation belt electrons through interaction with multi-subpacket chorus waves. *Earth Planets Space* **72**, 21. <https://doi.org/10.1186/s40623-020-1134-3>
- Hsieh YK, and Omura Y (2018). Nonlinear damping of oblique whistler mode waves via Landau resonance. *J Geophys Res Space Phys*, 123, 7462–7472. <https://doi.org/10.1029/2018JA025848>
- Jaynes AN, Baker DN, Singer HJ, et al. (2015). Source and seed populations for relativistic electrons: Their roles in radiation belt changes. *J Geophys Res Space Phys*, 120, 7240–7254., <https://doi.org/10.1002/2015JA021234>
- Kletzing CA, et al, (2012), The Electric and Magnetic Field Instrument and Integrated Science (EMFISIS) on RBSP, *Space Sci Rev*, doi: 10.1007/s11214-013-9993-6.
- Mauk BH, et al. (2012), Science objectives and rationale for the Radiation Belt Storm Probes mission, *Space Sci Rev*, doi:10.1007/s11214-012-9908-y.
- Omura Y, Nunn D (2011) Triggering process of whistler mode chorus emissions in the magnetosphere. *J Geophys Res* 116:A05205. <https://doi.org/10.1029/2010JA016280>
- Omura Y, Katoh Y, Summers D (2008) Theory and simulation of the generation of whistler-mode chorus. *J Geophys Res* 113:A04223. <https://doi.org/10.1029/2007JA012622>
- Omura Y, Hikishima M, Katoh Y, et al. (2009) Nonlinear mechanisms of lower-band and upper-band VLF chorus emissions in the magnetosphere. *J Geophys Res* 114:A07217. <https://doi.org/10.1029/2009JA014206>
- Omura Y, Hsieh YK, Foster JC, et al. (2019) Cyclotron acceleration of relativistic electrons through Landau resonance with obliquely propagating whistler mode chorus emissions. *J Geophys Res Space Phys* 124:2795–2810. <https://doi.org/10.1029/2018JA026374>
- Reeves GD, Spence HE, Henderson MG, et al. (2013), Electron acceleration in the heart of the Van Allen radiation belts, *Science*, doi:10.1126/science.1237743.
- Santolik, O, Gurnett, Pickett JS, et al. (2003), Spatio-temporal structure of storm-time chorus, *J Geophys Res*, 108 (A7), p. 1278, [10.1029/2002JA009791](https://doi.org/10.1029/2002JA009791)
- Santolik, O, Gurnett, Pickett JS, et al. (2004), A microscopic and nanoscopic view of storm-time chorus on 31 March 2001, *Geophys Res Lett*, 31 (2004), p. L02801, [10.1029/2003GL018757](https://doi.org/10.1029/2003GL018757)
- Santolik, O, Gurnett DA, Pickett JS, et al. (2009), Oblique propagation of whistler mode waves in the chorus source region, *J. Geophys. Res.*, 114, A F03, doi:10.1029/2009JA014586.

Santolík O, Kletzing CA, Kurth WS, et al., (2014), Fine structure of large-amplitude chorus wave packets, *Geophys Res Lett*,41,293–299,doi:10.1002/2013GL058889.

Shoji M, Omura Y (2013) Triggering process of electromagnetic ion cyclotron rising tone emissions in the inner magnetosphere. *J Geophys Res Space Phys* 118:5553–5561. <https://doi.org/10.1002/jgra.50523>

Thorne RM, Li W, Ni B, et al., (2013), Rapid local acceleration of relativistic radiation belt electrons by magnetospheric chorus, *Nature*, 504, 7480, 411–414, doi: 0.1038/nature12889.

Tsurutani BT, Chen R, Gao X, et al. (2020), Lower-band “monochromatic” chorus riser subelement/wave packet observations, *J Geophys Res Space Phys*,125, e2020JA028090, <https://doi.org/10.1029/2020JA028090>.

Zhang XJ, Mourenas D, Artemyev AV, et al., (2020). Rapid frequency variations within intense chorus wave packets. *Geophys Res Lett*, 47, e2020GL088853. <https://doi.org/10.1029/2020GL088853>

Tables

Table 1. Subpacket Characteristics

Parameter	A) 16:46:43 UT	B) 16:46:43 UT	C) 22:48:20 UT	D) 22:48:20 UT
L	5.13	5.13	6.49	6.49
f_{ce}	5325 Hz	5325 Hz	3310 Hz	3310 Hz
n_e	3 cm^{-3}	3 cm^{-3}	12 cm^{-3}	12 cm^{-3}
f_{pe}	15500 Hz	15500 Hz	31500 Hz	31500 Hz
f_{pe}/f_{ce}	2.91	2.91	9.51	9.51
magnetic latitude	-4.17	-4.17	-2.54	-2.54
# cycles	46	21	55	19
duration	39 ms	16 ms	73 ms	21 ms
f_{ceEQ}	4200 Hz	4200 Hz	2900 Hz	2900 Hz
f / f_{ce}	.206 - .225	.225 - .261	.208 - .234	.218 - .298
f / f_{ceEQ}	.277 - .303	.303 - .351	.246 - .277	.258 - .352
$ E_R \text{ max}$	20 mV/m	50 mV/m	6 mV/m	32 mV/m
$E_{res} (n = 1)$	60 keV	52 keV	10 keV	9 keV
500 keV % Gain	2.45	5.22	2.30	1.38
1 MeV % Gain	1.65	2.91	1.04	0.62

Figures

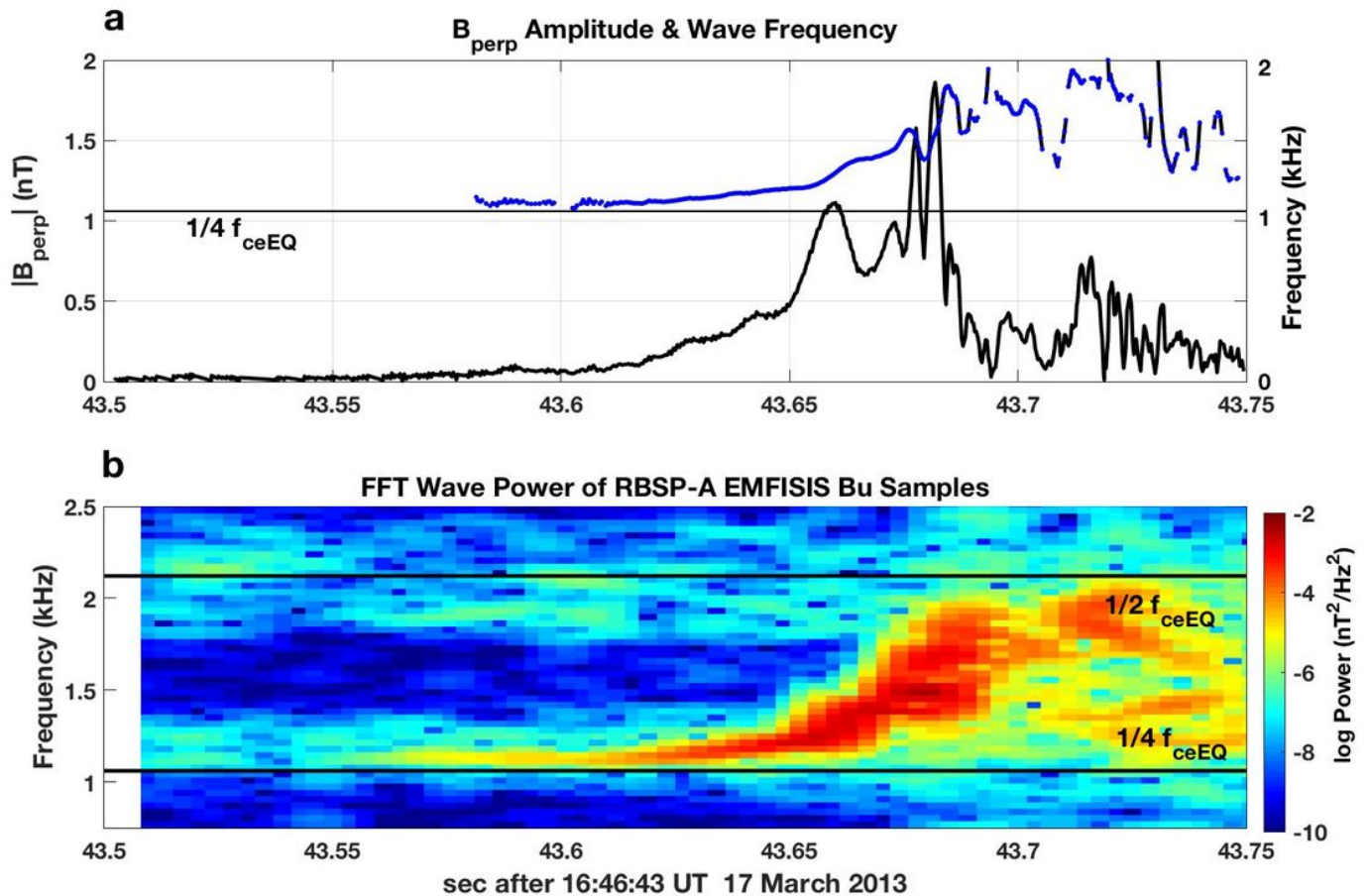


Figure 1

The analysis of Van Allen Probes EMFISIS high frequency wave magnetic field observations of a strong VLF chorus element observed during the 17 March 2013 event reveals the typical subpacket structure and relationship between wave amplitude and frequency. The RBSP-A spacecraft was at $L \sim 5$, ~ 02 MLT, and at a position ~ 4 deg off the equatorial plane. (a). Wave frequency (blue) and perpendicular wave magnetic field amplitude (black) are shown across the multiple subpackets comprising the chorus element. (b). The wave magnetic field spectrogram shows an extended (> 80 ms) period of gradually increasing wave power and frequency before the onset of the first strong subpacket at 43.65 s.

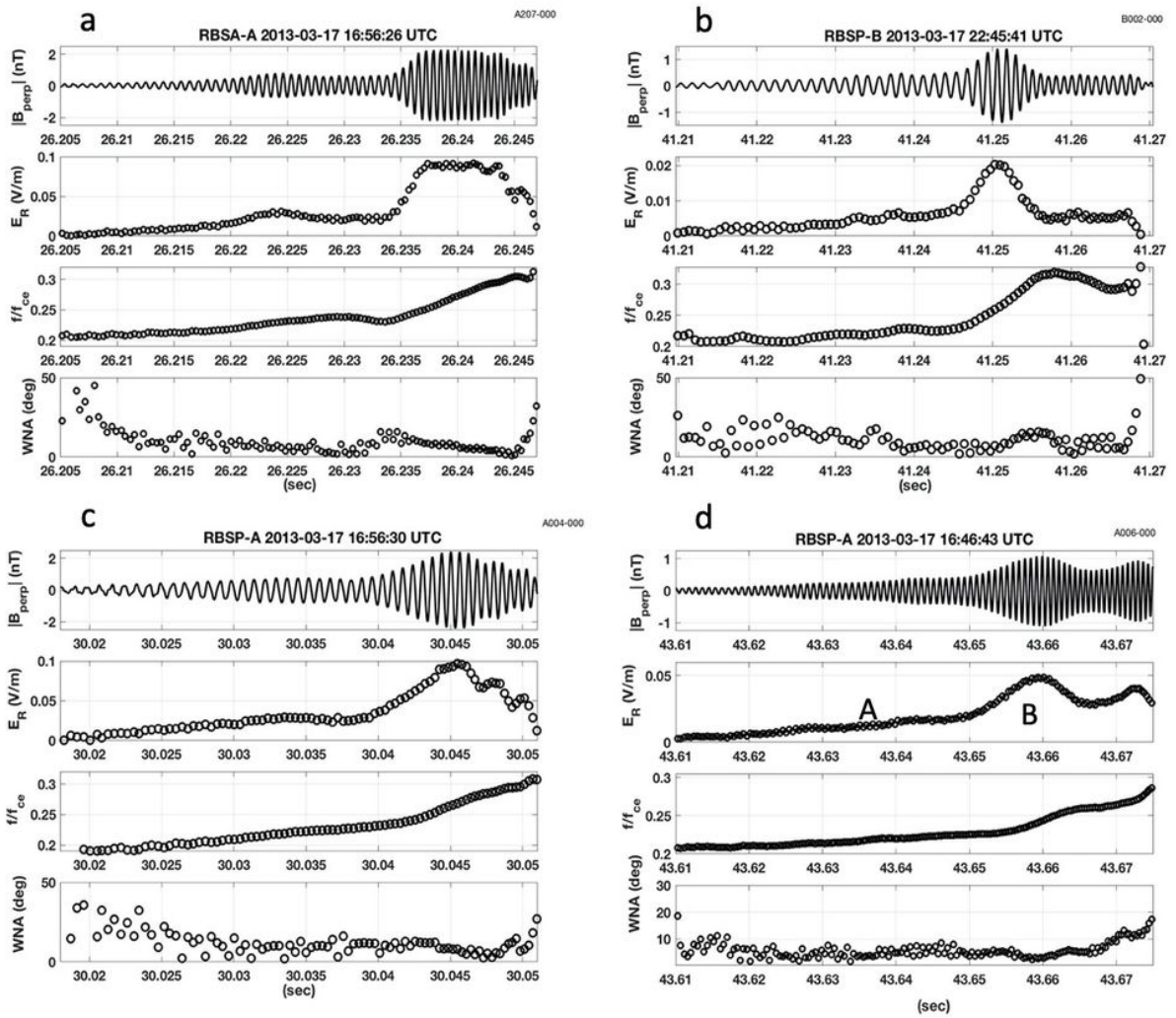


Figure 2

Detailed observations of the initial two subpackets of four strong chorus wave elements recorded during the March 17, 2013 event are shown in panels a, b, c, and d. See text for description. Panel b displays the analysis for the chorus element shown in Figure 1.

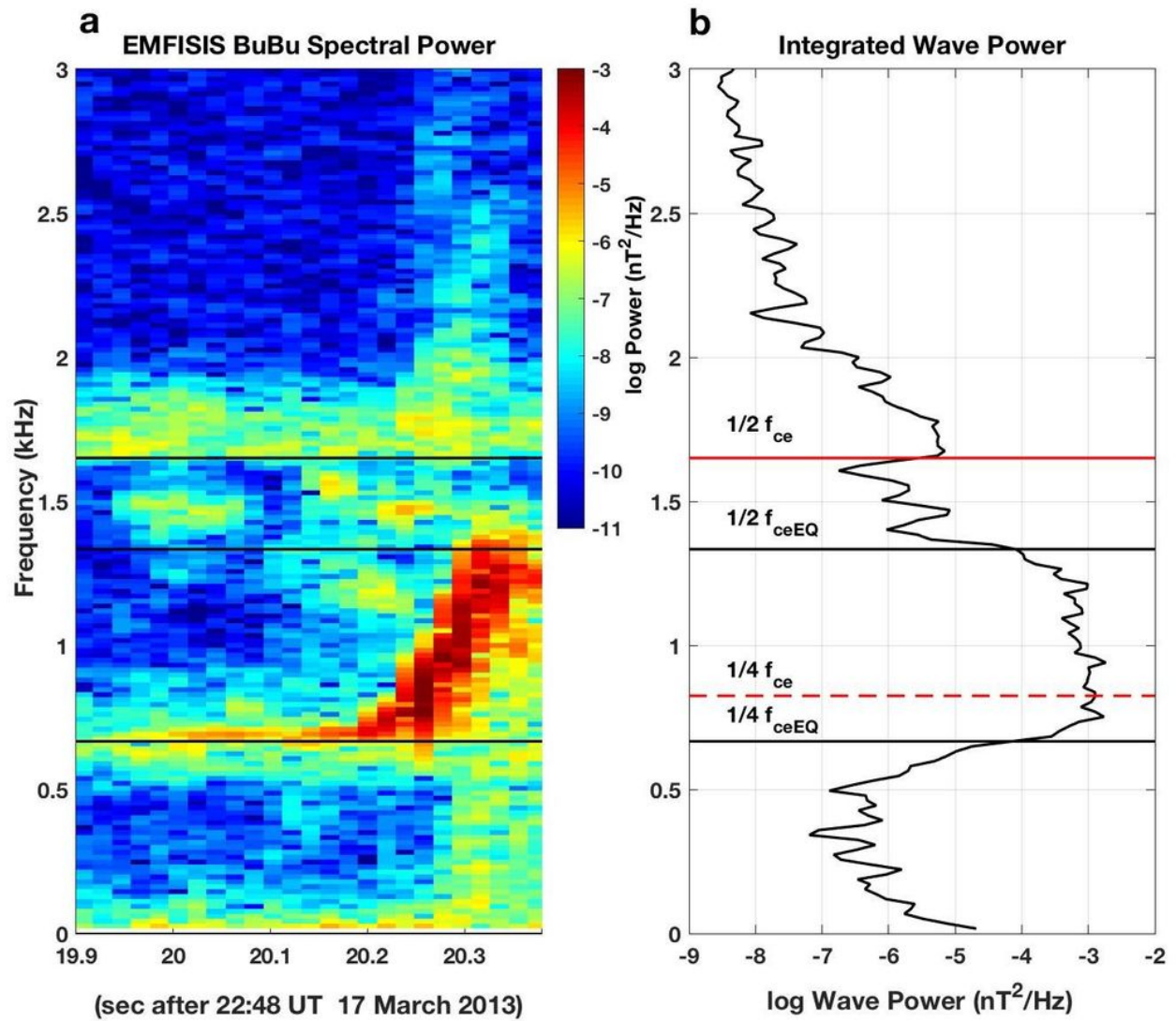


Figure 3

(a) The magnetic field spectrogram observed near L=6.5 by Van Allen Probe B at 22:48:20 UT on 17 March 2013 exhibited clear damping at frequencies below $1/2$ the local electron cyclotron frequency. (b) Integrated signal power at each frequency is shown for the ~ 400 ms of observations shown in panel (a). The local value of f_{ce} is observed at the spacecraft and the equatorial value of f_{ce} is determined from the characteristics of the damping of the chorus element.

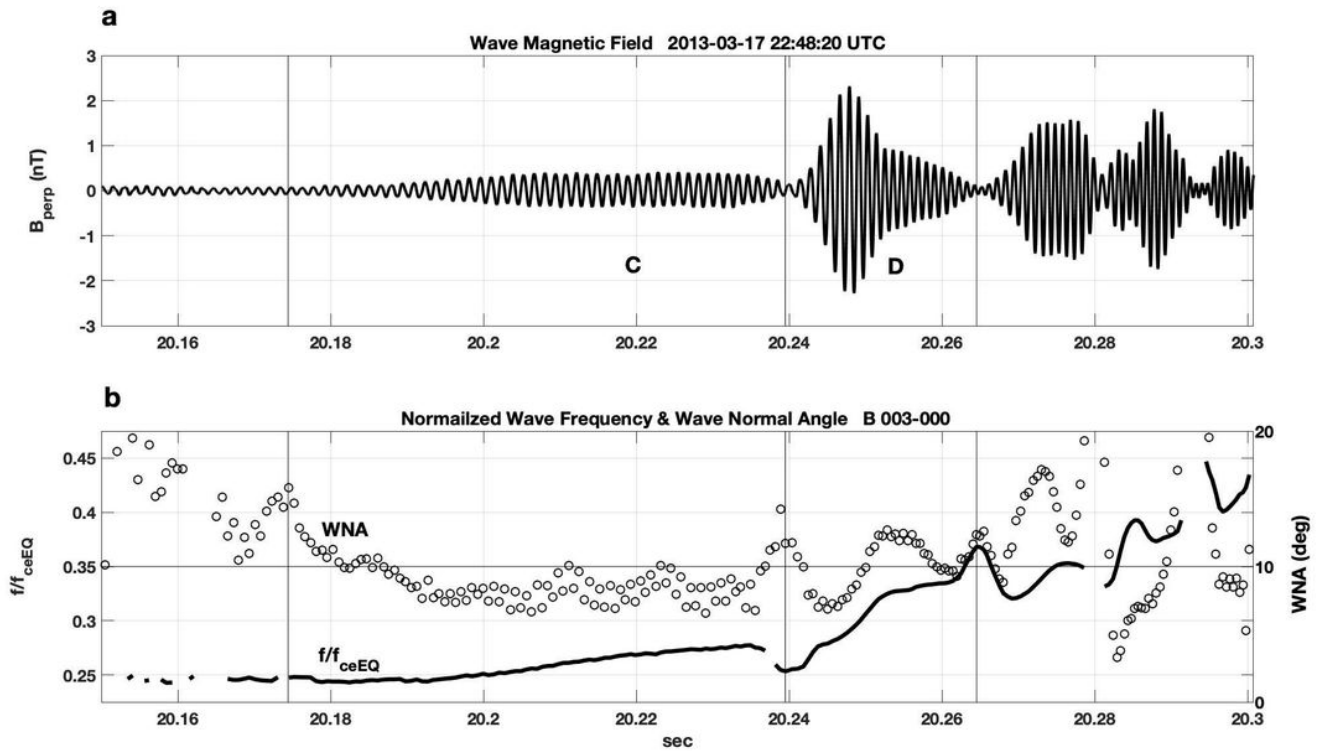


Figure 4

Analysis of the subpacket structure for the chorus element shown in Figure 3 is shown. (a). Wave magnetic field exhibits an initial gradual increase in amplitude over < 70 ms, followed by a second strong subpacket with $|B_{\text{perp}}| \sim 2$ nT. (b). Normalized wave frequency (solid line, f / f_{ceEQ}) and wave normal angle (open circles) are shown. Increasing wave amplitude and frequency are seen for $\text{WNA} < 10$ deg.

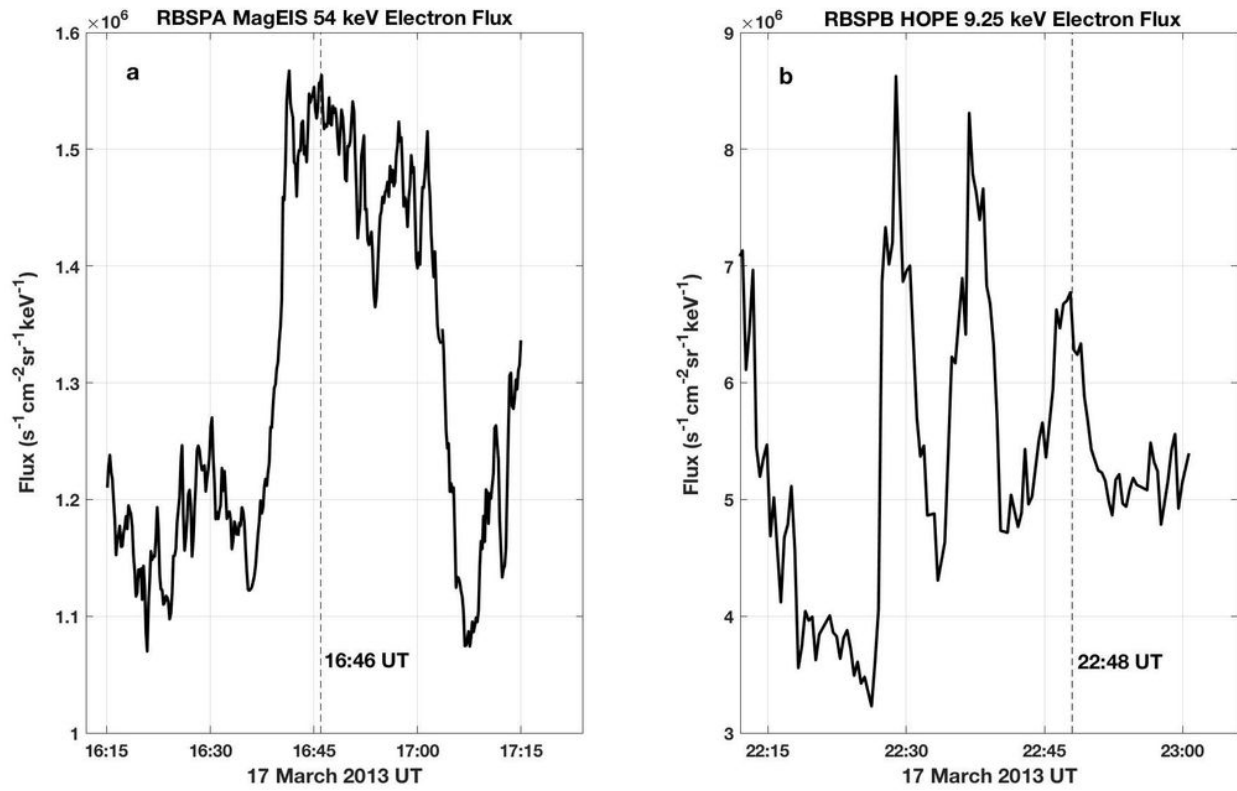


Figure 5

Sharp electron injections occurred at the ($n = 1$) cyclotron resonant energies associated with the growth of the chorus elements shown in Figure 2 (a. MagEIS 54 keV electrons) and Figure 4 (b. HOPE 9.25 keV electrons). The observation times of the chorus rising tones are indicated by dashed lines.

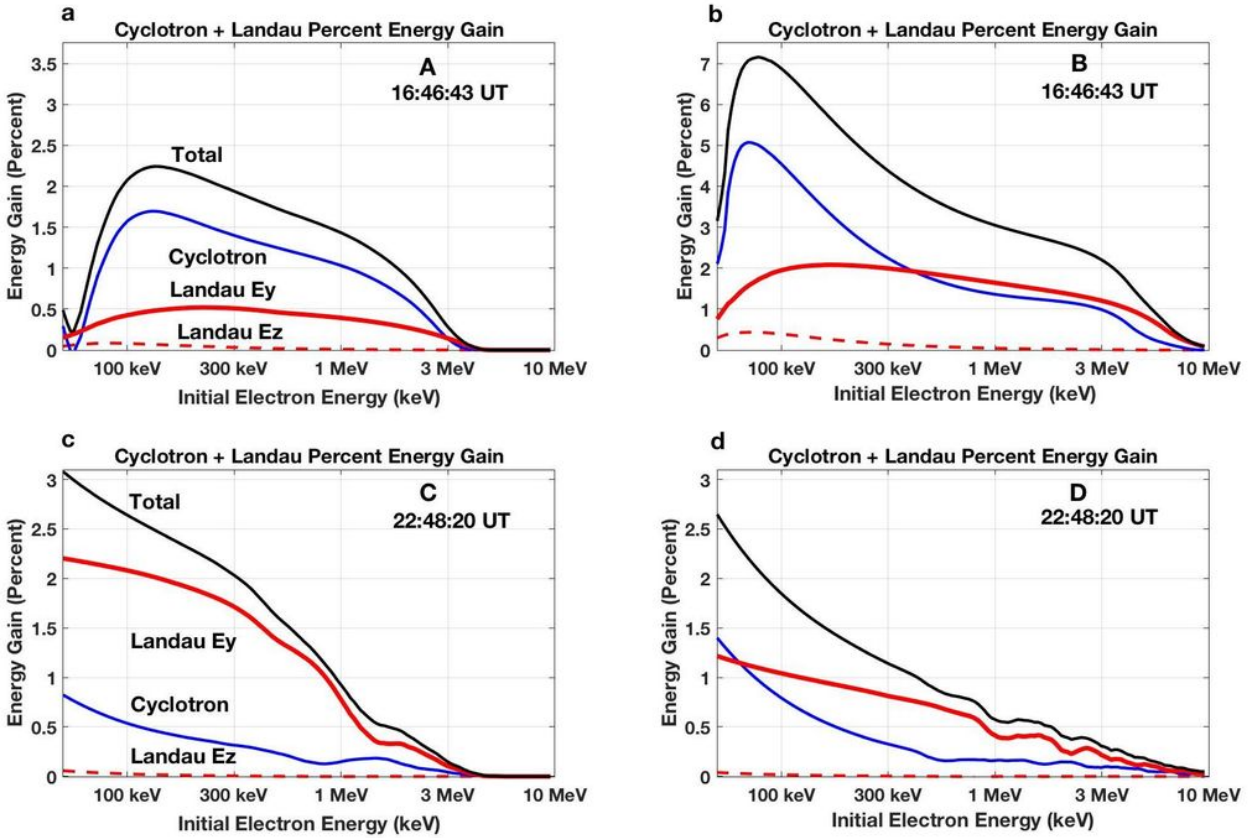


Figure 6

For obliquely-propagating chorus waves, the nonlinear Lorentz force of the perpendicular wave magnetic field result in effective electron acceleration. The percent energy gained by seed electrons in a resonant interaction with a single chorus subpacket is shown following the calculations of Omura et al. (2019). Panel a - d give the separate results for the initial (A and C) and 2nd strong (B and D) subpackets of the chorus elements described in Figures 2d (A and B) and 4 (C and D). Percent energy gain through the perpendicular Landau ($n = 0$) resonance is shown in red, through cyclotron ($n = 1$) resonance in blue, with the total gain shown in black.

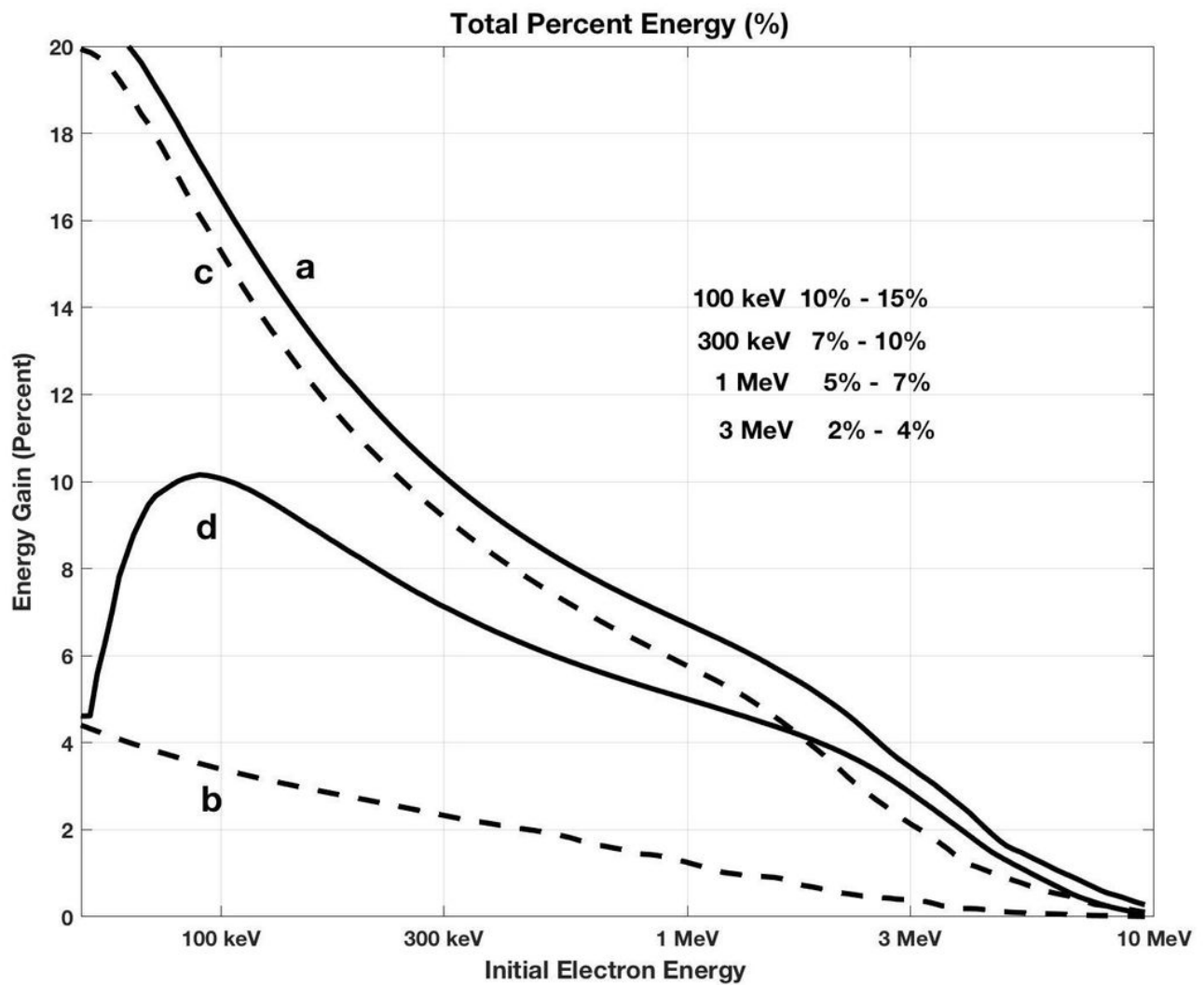


Figure 7

Percent energy gain is shown for seed electrons with initial energies between 30 keV and 10 MeV trapped in a single nonlinear interaction with the first two subpackets of the chorus elements shown in Figure 2 panels (a, b, c, d) following the calculations of Omura et al. (2019).

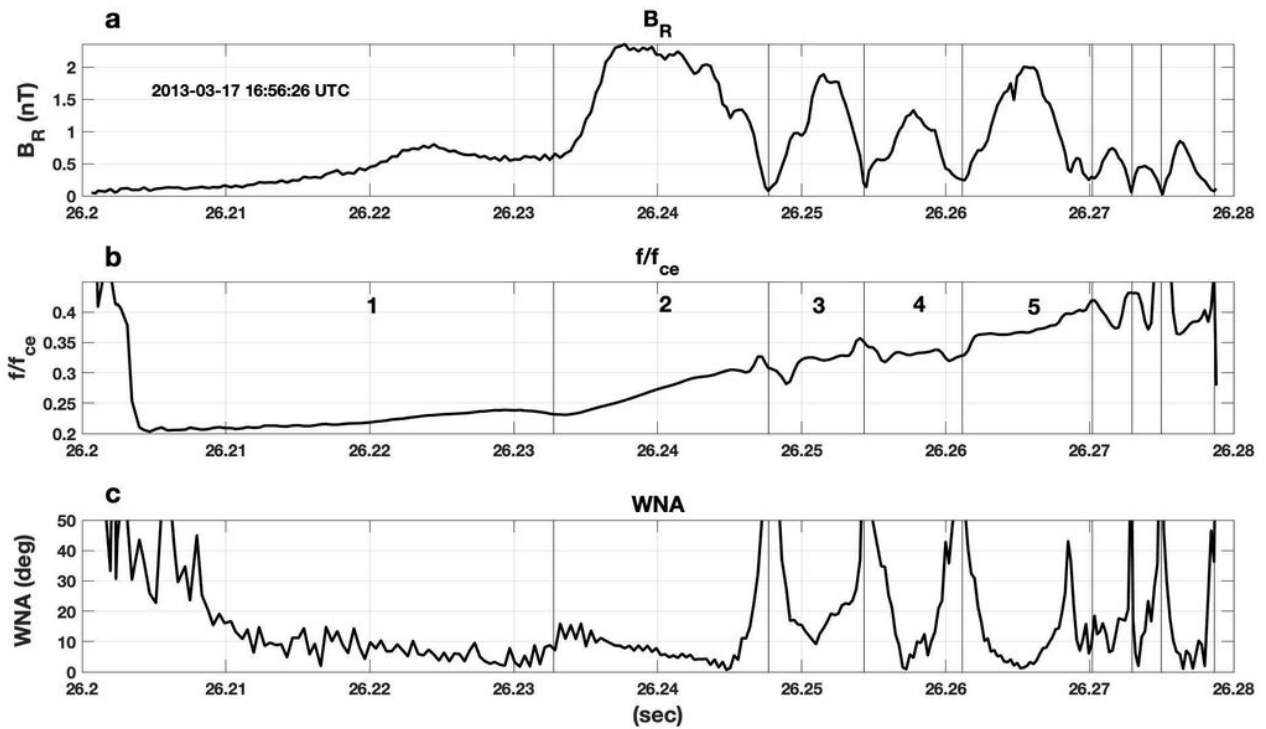


Figure 8

For the chorus element shown in Figure 2a, panel (a) presents the right-hand mode wave magnetic field amplitude (B_R), (b) normalized wave frequency, and (c) wave normal. The initial 5 subpackets are indicated with vertical lines. The long-duration subpackets (1, 2, and 5) exhibit smoothly rising frequency across their temporal extent while a step-like frequency plateau characterizes the shorter subpackets (3 and 4).

Supplementary Files

This is a list of supplementary files associated with this preprint. Click to download.

- [FosterGraphicsAbstract.pdf](#)